



Bi- and trimetallic Ni catalysts over Al₂O₃ and Al₂O₃-MO_x (M = Ce or Mg) oxides for methane dry reforming: Au and Pt additive effects



Hongjing Wu^{a,b}, Giuseppe Pantaleo^a, Valeria La Parola^a, Anna M. Venezia^a,
Xavier Collard^c, Carmela Aprile^c, Leonarda F. Liotta^{a,*}

^a Institute for The Study of Nanostructured Materials (ISMN)-CNR, Palermo 90146, Italy

^b Department of Applied Physics, Northwestern Polytechnical University (NPU), Xi'an 710072, PR China

^c Department of Chemistry, University of Namur (UNAMUR), 61 rue de Bruxelles, B-5000 Namur, Belgium

ARTICLE INFO

Article history:

Received 14 December 2013

Received in revised form 4 March 2014

Accepted 11 March 2014

Available online 21 March 2014

Keywords:

Dry reforming

Trimetallic catalysts

Synergistic interaction NiAuPt

Bamboo-like carbon nanotubes

ABSTRACT

The effects of Au and Pt addition (in very low concentrations, 0.2 wt%) on the catalytic performances of 4 wt% Ni catalysts supported over Al₂O₃ and Al₂O₃-10 wt%MO_x (M = Ce or Mg) oxides were studied in the dry reforming of methane (DRM). The properties of the catalysts, before and after long-run tests, were investigated employing N₂ adsorption-desorption isotherms, XRD, H₂-TPR, XPS, TEM, EDX microanalysis and O₂-TPO. It was shown that addition of a small amount of Au and Pt (0.2 wt%) to Ni catalyst leads to formation of a synergistic interaction, which induces easy reduction of NiO species and decrease of particle size. It was also found that the small amount of Au and Pt addition plays an important role on catalytic performance of bi-/trimetallic catalysts and carbon poisoning. The improvement of catalytic activity and stability obtained for the trimetallic NiAuPt/Al₂O₃ catalyst was attributed to the formation of high active Ni-Au-Pt nanoparticles, synergistically interacting, where growth of small amount of bamboo-like carbon nanotubes occurs. Conversely, abundant amorphous carbon and both, amorphous and carbon nanotubes, were detected in the bimetallic, NiAu and NiPt, and monometallic Ni alumina supported catalysts.

The effect of Al₂O₃ doping with MgO or CeO₂ also significantly improves the catalytic performance of monometallic Ni catalyst and the nature and amount of carbon deposits as well. However, the support effect was weakened in both Mg and Ce doped trimetallic catalysts due to the dominant role of Ni-Au-Pt interaction responsible of the enhanced activity for DRM.

© 2014 Elsevier B.V. All rights reserved.

1. Introduction

Since 1993, production of hydrogen *via* dry reforming of methane (DRM) and other light hydrocarbons and followed water-gas shift reaction have received much attention because of the utilization of two important greenhouse gases, *i.e.*, CH₄ and CO₂. Nickel is the most frequently reported metal in DRM because of its good catalytic activity and its cost-effectiveness as compared with Pt, Ru or Rh-based catalysts [1,2]. Al₂O₃-supported Ni catalysts prepared by wetness impregnation have been widely investigated for DRM because of its high initial conversion, which however decreased with time due to carbon deposition or sintering. To overcome this problem many modification methods have been studied to improve the performance of Ni/Al₂O₃ catalysts, which include different preparation methods, pre-treatments and precursors, or

adding metal or oxide promoters to influence the acidity-basicity, the dispersion of Ni, and/or the metal-support interaction [3,4].

It is well known that bimetallic catalysts may sometimes exhibit superior activity, selectivity and deactivation resistance compared with those of the corresponding monometallic ones. It has been reported that noble metals inhibit coke deposition, and affect the type of carbon at formed over Ni catalysts [5–9]. Moreover, a small amount of noble metals can promote the reducibility of Ni, and stabilize it against sintering [1–4]. Therefore, recently, attempts have been made to modify the Ni catalysts by adding a second metal such as Pt or Au to Ni [5–9]. Aksoylu and co-worker [5] studied a series of Pt-Ni bimetallic catalysts supported on δ -Al₂O₃ to be used in DRM. They found that 0.3 wt%Pt-10 wt%Ni/Al₂O₃, with the highest Pt/Ni loading ratio in the series, exhibited the highest catalytic activity and stability. García-Diéguez *et al.* [6] observed that Pt improved CH₄ and CO₂ conversion and enhanced the stability of Ni/nanofibrous Al₂O₃ for DRM. Furthermore, they reported the formation of Pt/Ni alloy, Pt enriched at the surface and with smaller metal crystal size as compared to monometallic Pt and Ni

* Corresponding author. Tel.: +39 091 6809 371; fax: +39 091 6809 399.
E-mail address: liotta@pa.ismn.cnr.it (L.F. Liotta).

catalysts, associated with higher activity and lower coke formation upon DRM [7]. Nevertheless, the catalytic stability of catalysts with Pt/Ni weight ratios of 0.4 and 0.04 was quite similar in spite of the fact that the carbon deposition was significantly different. This suggests that a very small amount of Pt can promote DRM. On the other hand, Guzzi et al. [8] investigated the promoting effect of Au on catalytic performance of 8.8 wt%Ni/MgAl₂O₄ for DRM with a mixture of 29 vol%CO₂ and 71 vol%CH₄. They found that the 0.5 wt% Au hampered the DRM but on long range the activity was improved in the presence of gold. Recently, with the same reagent mixture, we found that the monometallic nickel catalyst was more active at lower temperature whereas the Au–Ni bimetallic catalysts were more active at higher temperature [9]. It is reported in literatures that support has a significant effect on both catalytic activity and stability [10–12]. An appropriate support should be able to improve the dispersion of active components, promote effective metal-support interactions, and retain the unique properties of the impregnated metals [13–15]. It has been shown that ZrO₂ and CeO₂ supports are able to provide oxygen to the metal during the reaction and suppress carbon deposition [12,16–19], owing to its unique acid–base and redox properties, reducibility and high thermal stability. Thus, oxides with high oxygen exchange capacity and mobility are expected to be excellent candidates as support promoters for DRM. Moreover, the addition of a basic metal oxide (e.g., MgO) improved the coke resistance of a DRM catalyst [20]. In this case, the suppression of coke results from the increase of CO₂ adsorption and decrease of CH₄ decomposition [21–25]. Besides, over the past decades, Ni/MgO catalyst obtained from NiO–MgO solid solution has been attracting renewed interest due to its high stability in long-run DRM reaction [3,4,26–29]. The authors suggested that the excellent activity and high stability of the reduced NiO–MgO catalyst depended on their composition, preparation conditions and properties of the support. However, poor results were obtained over the catalyst with Ni loading as low as 4 wt% [27–29]. Until now, few researches on Pt–Au–Ni trimetallic catalysts for DRM have been reported. Aksoylu et al. [30] have found an optimum catalyst composition of 0.3 wt%Pt–15 wt%Ni/Al₂O₃ for oxidative steam reforming (OSR) of propane but the presence of 0.3 wt%Au in the trimetallic catalyst caused a poor activity and selectivity in comparison to bimetallic catalysts. The aim of the present work is to develop effective bi-/trimetallic 4 wt%Ni catalysts with a very small amount of metals (0.2 wt% Pt and/or Au) with improved resistance to coke deposition and good performance for DRM. The effect of the Al₂O₃ support doping with MgO or CeO₂ via sol–gel method on catalytic performance of Ni-based catalysts was also investigated. The catalysts were characterized by various physicochemical methods. Their catalytic activity and long-run stability were evaluated under DRM conditions at steady state.

2. Experimental

2.1. Catalyst preparation

All the used reagents (Sigma-Aldrich) were of analytical grade.

2.1.1. Preparation of Al₂O₃ and Al₂O₃–10 wt%MO_x (M = Ce or Mg) oxides

Al₂O₃ and Al₂O₃–10 wt%MO_x (M = Ce or Mg) supports were prepared using classical sol–gel method. A typical preparation of Al₂O₃–10 wt%MO_x (M = Ce or Mg) is the following: Al[OCH(CH₃)C₂H₅]₃ was dissolved in sec-butyl alcohol at 40 °C for 30 min. Second, Ce(NO₃)₃·6H₂O or Mg(NO₃)₂·6H₂O dissolved in water was added dropwise under vigorous stirring and then left for 30 min. Third, HNO₃ (65 wt%) solution was added to the previous mixture until pH 3. Finally, the suspension was refluxed for 2 h at

Table 1

Chemical composition of the Ni-based catalysts.

Catalysts	Metals (Ni/Au/Pt) loadings (wt%)	MgO/CeO ₂ loadings (wt%)
NiAl	4% Ni	–
NiAlMg	4% Ni	10% MgO
NiAlCe	4% Ni	10% CeO ₂
NiAuAl	4% Ni–0.2% Au	–
NiPtAl	4% Ni–0.2% Pt	–
NiAuPtAl	4% Ni–0.2% Au–0.2% Pt	–
NiAuPtAlMg	4% Ni–0.2% Au–0.2% Pt	10% MgO
NiAuPtAlCe	4% Ni–0.2% Au–0.2% Pt	10% CeO ₂

60 °C and submitted to hydrothermal treatment at 100 °C for 43 h. After cooling, the resulting mixture was filtered, washed, dried at 100 °C overnight and then calcined by heating the solid at 800 °C for 6 h under static air.

In the catalyst notation the pure alumina is indicated as Al and the Mg and Ce doped supports are indicated as AlMg and AlCe.

2.1.2. Preparation of monometallic, bimetallic and trimetallic catalysts

Monometallic 4 wt%Ni catalysts were prepared through wetness impregnation method of the above-mentioned supports with Ni(NO₃)₂·6H₂O aqueous solution at r.t. The solid was then dried at 100 °C overnight and calcined at 550 °C for 5 h under static air. 0.2 wt%Au (HAuCl₄ as precursor) or 0.2 wt% Pt (Pt(NH₃)₄(NO₃)₂ as precursor) was deposited over the monometallic Ni catalysts using deposition–precipitation (Dp) or impregnation method, respectively. The Dp samples, i.e., Au–Ni bimetallic catalysts were prepared as follows: the monometallic Ni catalyst was suspended under stirring in water, to which an appropriate volume of HAuCl₄ solution (1.27×10^{-2} M) to yield the desired noble metal loading was added. Urea was then added heating up to 90 °C and kept refluxing under stirring overnight (final pH 7.5–8). The sample was then cooled down to room temperature, filtered and washed with water until no chloride ions were detected by the AgNO₃ test. The presence of any gold species in the filtrate solution was checked by SnCl₂ test. The catalyst was dried in static air at 100 °C overnight and calcined at 400 °C for 2 h. The Pt–Ni bimetallic catalysts were done by wetness impregnation at r.t, dried at 100 °C overnight and calcined at 400 °C for 2 h. The Pt–Au–Ni trimetallic catalysts were synthesized by impregnating the as-prepared Au–Ni bimetallic catalysts (without calcination) with 0.2 wt%Pt, using an appropriate volume of Pt(NH₃)₄(NO₃)₂ solution (5×10^{-3} M). The catalyst was then dried at 100 °C overnight and calcined at 400 °C for 4 h. The list of the prepared samples is given in Table 1. In Fig. 1, a simplified scheme for the preparation of all catalysts investigated is reported.

2.2. Characterization

2.2.1. Elemental analysis

Elemental analysis of the catalysts was performed by inductively coupled plasma optical emission spectroscopy (ICP-OES), using an ICP Perkin-Elmer Optima 3000DV spectrometer. The powders were firstly dissolved in acidic medium (H₂SO₄/HNO₃/HF) evaporated until dryness and then again dissolved in aqua regia. The real composition of the catalysts corresponded to the nominal content within ±5%.

2.2.2. X-ray diffraction (XRD)

XRD measurements were carried out with a Bruker D 5000 diffractometer equipped with a Cu K α anode and a graphite

monochromator. A proportional counter and a 0.05° step size in 2θ were used. The assignment of the various crystalline phases in 2θ was based on the JCPDS powder diffraction file cards [31]. The particle size (d) was estimated as volume-average crystallite dimension, through the line-broadening (LB) of the available reflection peaks, using the Scherrer equation [32]. The instrumental broadening was determined by collecting the diffraction pattern of the standard, lanthanum hexaboride LaB_6 .

2.2.3. BET analyses

Specific surface area (SSA) measurements were performed using a Sorptomatic 1900 Carlo Erba Instrument, by physical adsorption of N_2 at the temperature of liquid nitrogen (-196°C), using the BET method in the standard pressure range of $0.05\text{--}0.30\text{ p/p}_0$. By analysis of the desorption curve, by applying the BJH calculation method, the pore size distribution and pore volume were also obtained [33].

2.2.4. Transmission electron microscope (TEM)

TEM images were obtained using a FEI Tecnai 10 system with an operating voltage of 80 kV. Samples were dispersed in absolute alcohol and deposited on a carbon coated copper grid.

2.2.5. Energy dispersive X-ray (EDX) microanalysis realized with SEM

Chemical composition of all catalysts was determined by an energy-dispersive X-ray microanalysis realized with scanning electron microscope (SEM) using a JEOL JSM 7500 with conventional sample preparation and using an acceleration potential of 7.5 kV and a working distance of 8 mm. Transmission electron microscopy (TEM) images were obtained using a Philips Tecnai 10 with an accelerating voltage of 80 kV.

2.2.6. Temperature programmed reduction/oxidation (H_2 -TPR/ O_2 -TPO)

Temperature programmed reduction (TPR) experiments were carried out with a Micromeritics Autochem 2950 apparatus equipped with a thermal conductivity detector (TCD). The gas mixture with composition H_2 (5 vol% in Ar, 30 mL min^{-1}) is used to reduce the samples (50 mg), heating from room temperature to 750°C at the rate of $10^\circ\text{C min}^{-1}$. The catalyst powders were sieved using the fraction between 180 and $250\text{ }\mu\text{m}$ checking for the absence of mass transfer limitations [34]. Before starting the TPR analyses, the catalysts were pretreated with a flowing gas mixture of 5% O_2 in He (50 mL min^{-1}) at 550°C for 30 min, then cooling down under He. The amount of carbon on the sample surface after catalytic tests was estimated from the amount of CO_2 evolved in temperature programmed oxidation (TPO) experiments carried out with O_2 (5 vol% in He, 30 mL min^{-1}). Mass spectrometer was employed to detect CO_2 formation.

2.2.7. X-ray photoelectron spectroscopy (XPS)

The X-ray photoelectron spectroscopy (XPS) analyses were performed with a VGMicrotech ESCA 3000Multilab, equipped with a dual Mg/Al anode. The analyses were registered over selected catalysts after calcinations at 550°C . Moreover, in order to get insights into the ageing and poisoning of used catalysts, the analyses were performed over the same samples after long-run tests. No data over reduced catalysts were reported hereinafter because of the impossibility to reduce “in situ” the Ni catalysts before XPS measurements.

The spectra were excited by the unmonochromatized Al $K\alpha$ source (1486.6 eV) run at 14 kV and 15 mA. The analyser was operated in the constant analyser energy (CAE) mode. For the individual peak energy regions, a pass energy of 20 eV set across the hemispheres was used. Survey spectra were measured at 50 eV pass energy. The sample powders were mounted on a double-sided

adhesive tape. The pressure in the analysis chamber was in the range of 10^{-8} Torr during data collection. The constant charging of the samples was removed by referencing all the energies to the Al 2p set at 74.5 eV. The invariance of the peak shapes and widths at the beginning and at the end of the analyses ensured absence of differential charging. Analyses of the peaks were carried out with the software provided by VG, based on non-linear least squares fitting program using a weighted sum of Lorentzian and Gaussian component curves after background subtraction according to Shirley and Sherwood [35,36]. Atomic concentrations were calculated from peak intensity using the sensitivity factors provided with the software. The binding energy values are quoted with a precision of $\pm 0.15\text{ eV}$ and the atomic percentage with a precision of $\pm 10\%$.

2.3. DRM reaction

Activity tests were carried out in a U-shaped fix-bed reactor with an inner diameter of 12 mm, electrically heated in a furnace. 50 mg of catalyst as powder (sieved fraction between 180 and $250\text{ }\mu\text{m}$) was placed on a porous quartz disk. The reaction temperature as obtained by a K-type thermocouple in contact with the catalytic bed, long 12 mm. Before reaction, catalysts were pretreated *in situ* with 5 vol% O_2/He at 350°C , 30 min, then reduced with 5 vol% H_2/Ar from room temperature up to 750°C (heating rate $10^\circ\text{C min}^{-1}$) for 1 h.

The standard reagent gas mixture consisting of 15 vol% CH_4 + 15 vol% CO_2 in He was led over the catalyst at a flow rate of 50 mL min^{-1} (STP), equivalent to a weight hourly space velocity (WHSV) of $60,000\text{ mL g}^{-1}\text{ h}^{-1}$. The catalytic conversions were measured by increasing the temperature from 400 to 850°C (by steps of 50°C , hold time 30 min at target temperature). After catalytic run in the range of temperature 400– 800°C , the catalyst was left under the reaction mixture at 750°C for 24 h in order to check for time stability (herein called as long-term or long run tests).

The inlet and outlet gas compositions were continuously checked by two IR analysers (ABB Uras 14 and Uras 26) for CO, CO_2 and CH_4 , respectively. The above systems were calibrated for analyzing the gas concentration in different ranges: 0–10,000 ppm and 0–30 vol% for CO; 0–30 vol% for CO_2 ; 0–30,000 ppm and 0–30 vol% for CH_4 , respectively. Moreover, the evolution of all the species, CH_4 , CO, CO_2 , H_2 , H_2O was monitored by on line mass quadrupole (ThermostarTM, Balzers). Carbon balance was closed with deviation lower than 5% in all the catalytic tests.

The reproducibility of activity tests was confirmed by repeating three times each test. The obtained values differed of $\pm 3\%$, always confirming the trend of activity hereinafter reported.

3. Results and discussion

3.1. XRD characterization

The XRD patterns of selected calcined catalysts, NiAl, NiAlMg, NiAlCe, NiAuAl, NiPtAl and NiAuPtAl, are shown in Fig. 2. All catalysts present the characteristic feature of $\gamma\text{-Al}_2\text{O}_3$ phase (JCPDS 75-0921), with no peaks associated to NiO neither to NiAl_2O_4 (JCPDS 01-1299). The pattern of the NiAlMg sample, similarly to all the Mg doped catalyst, does not present any peaks related to MgO features (JCPDS 65-0476) neither to MgAl_2O_4 (10-0062) while the pattern of NiAlCe and of the other Ce doped samples contains the typical fluorite CeO_2 (JCPDS 34-0394) diffraction lines. As expected on the bases of the low noble metal content, the diffraction patterns of the bi and trimetallic samples did not contain any gold or platinum related peaks. The textural properties of the prepared catalysts and corresponding supports are summarized in Table S1. In Fig. S1 the isotherms of monometallic Ni catalysts are displayed

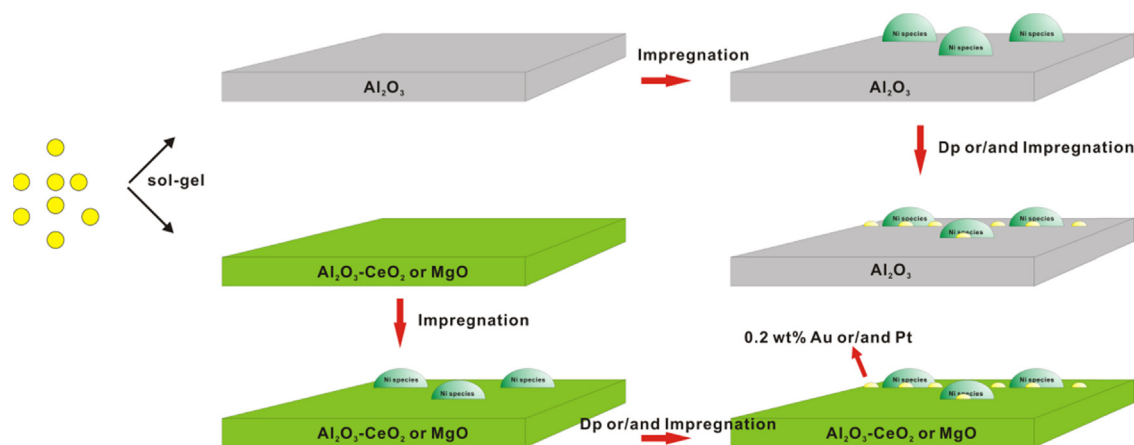


Fig. 1. Simplified scheme for the preparation of all the catalysts studied.

and compared with the alumina and doped-alumina oxides. The detected phases and average crystal sizes for the calcined catalysts are in detail listed in Table S2.

In order to investigate the structural modification induced by reduction pretreatment at 750 °C for 1 h, performed before the DRM reaction, selected catalysts were characterized by XRD immediately after reduction (see Fig. 3). In the pattern of the sample NiAl, the Ni(111) and Ni(200) peaks were clearly observed at $\sim 44.6^\circ$ and at $\sim 52^\circ 2\theta$, respectively. Quite interesting, the addition of Au or/and Pt or both metals leads to broadening of the Ni(200) peak along with a shift towards lower angles. No features of the Ni(111) appeared in the bi-/trimetallic catalysts probably because of two factors, signal broadening and overlapping with the alumina background. According to the Vegard's law the shift of the metal peaks in the bimetallic/trimetallic sample with respect to the pure metal position may suggest some bulk alloy formation and can be used to estimate the composition [37]. Therefore, from the differences of the lattice parameters, obtained from the Ni(200) peaks (the only one detectable) the composition of the alloy phase enriched in nickel ($\sim 98\text{at}\%$ for all bi- and tri-metallic samples) was approximately estimated. By applying the Scherrer equation, Ni^0 crystallites with an average diameter of 11.0 nm for NiAl and smaller ones ($\sim 6.1\text{--}6.6\text{ nm}$) for bi-/trimetallic catalysts were calculated (Table 2).

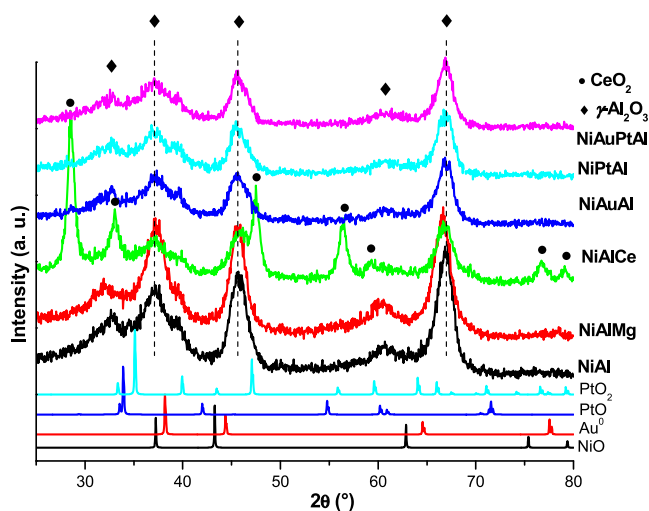


Fig. 2. XRD patterns of selected catalysts after calcination.

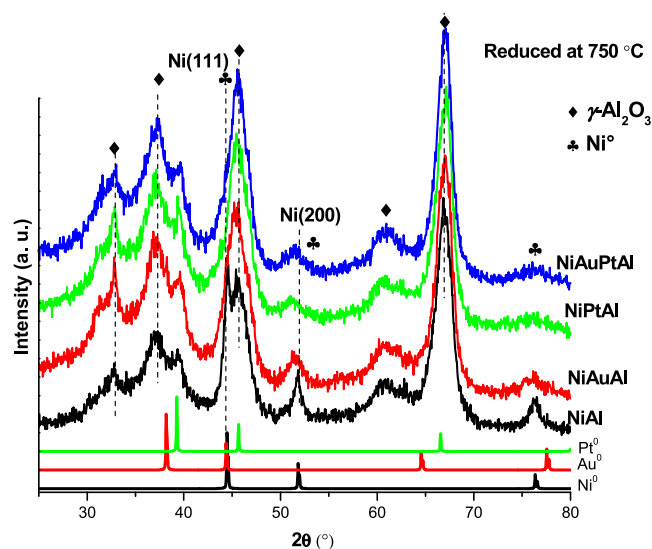


Fig. 3. XRD patterns of alumina supported Ni, NiAu, NiPt and NiAuPt catalysts after H_2 reduction treatment.

3.2. Reducibility of the calcined catalysts

Generally, H_2 -TPR is an effective technique for examining the reducibility of the catalysts. The H_2 -TPR profiles of the calcined catalysts are shown in Figs. 4 and 5. All the catalysts exhibited similar profiles of hydrogen reduction, exhibiting two pronounced reduction peaks with the peak maximum in the range of 291–466 °C (α peaks) and 684–751 °C (γ peaks), respectively. Interestingly, for NiAlCe and all trimetallic catalysts, a broad peak with peak maximum is observed at around 532–557 °C (β peaks). The first range of reduction peaks (α peaks) appear at relatively low temperatures and might be caused by the large particles of “free” Ni^0 , which although dispersed by the support, do not form chemical

Table 2

Shift of the Ni(200) reflection and average particle size of Ni enriched alloy phase (as estimated by XRD) for Ni and bi-/trimetallic (Au/Pt) Ni over alumina catalysts.

Catalysts	The shift of the Ni(200) reflection with the composition	Particle size (nm) ^a
NiAl-red	51.85	11.0
NiAuAl-red	51.50	6.6
NiPtAl-red	51.35	6.2
NiAuPtAl-red	51.45	6.1

^a Calculated through Ni(200) by Scherrer equation.

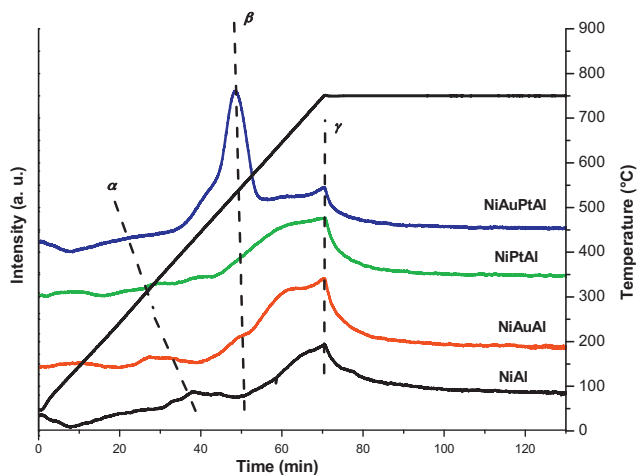


Fig. 4. TPR profiles of Ni, NiAu, NiPt and NiAuPt catalysts over alumina.

bonds with the underlying support surface [38]. The high temperature reduction peak (γ peak) at around 750 °C was attributed to Ni species strongly interacting with alumina [38].

The relatively high temperature reduction peaks (β peaks) might be assigned to the highly dispersed Ni^{2+} species interacting with support surface. The addition of Au or/and Pt could promote the reduction of Ni^{2+} because of the hydrogen spillover phenomenon. On the metallic surface, hydrogen molecules dissociate to hydrogen atoms, which are diffused to the Ni^{2+} and can react with NiO to consume the hydrogen. However, the rate of reduction of NiO depends not only on its chemical nature but also on nucleation process by which metallic nuclei are generated [38]. Compared with bimetallic catalysts, it can be assumed that the highly dispersed NiO in NiAuPtAl could be more easily reduced by hydrogen atoms from spillover effect due to the unique interaction among Ni, Au and Pt species and served as metallic nuclei to facilitate reduction of Ni^{2+} . In the case of the NiAlCe TPR, the presence of a peak at 557 °C close to the β peak observed in the trimetallic NiAuPtAl at 532 °C, attributed to highly dispersed NiO particles interacting with the support could rather be attributed to the reduction of CeO_2 with formation of CeAlO_3 as confirmed by the XRD of the samples after the reduction or reaction treatment (see later). Indeed such peak is not present in the NiAlMg TPR pattern, whereas is present in the patterns of the trimetallic NiAuPtAlCe as a low temperature shoulder of the β peak.

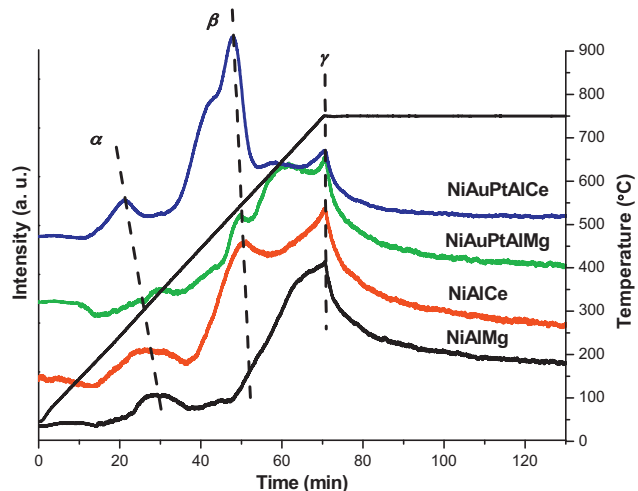


Fig. 5. TPR profiles of Ni and NiAuPt catalysts over alumina doped with Mg or Ce.

Table 3

H_2 -TPR quantitative analysis results for the catalysts.

Catalysts	α (°C)	β (°C)	γ (°C)	Total H_2 uptake ($\mu\text{mol g}^{-1}$)
NiAl	426	–	750	679
NiAlMg	324	–	751	680
NiAlCe	298	557	751	970
NiAuAl	327	–	751	688
NiPtAl	319	–	737	690
NiAuPtAl	245	532	750	700
NiAuPtAlMg	346	543	751	698
NiAuPtAlCe	251	524	751	988

Note: Theoretical H_2 uptake for 4% Ni is 681 $\mu\text{mol g}^{-1}$.

All the H_2 -TPR quantitative analysis results are listed in Table 3. The total H_2 consumption values are in accord with the theoretical H_2 uptake for 4%Ni, suggesting that the Ni^{2+} species are completely reduced. Reduction of any ionic Au and Pt species contributed very little ($\leq 20 \mu\text{mol g}^{-1}$) to the overall hydrogen consumption. The ceria is almost completely reduced in the surface and in the bulk increasing the values of total H_2 consumption of about 290 $\mu\text{mol g}^{-1}$ for Ni-based catalysts supported on AlCe.

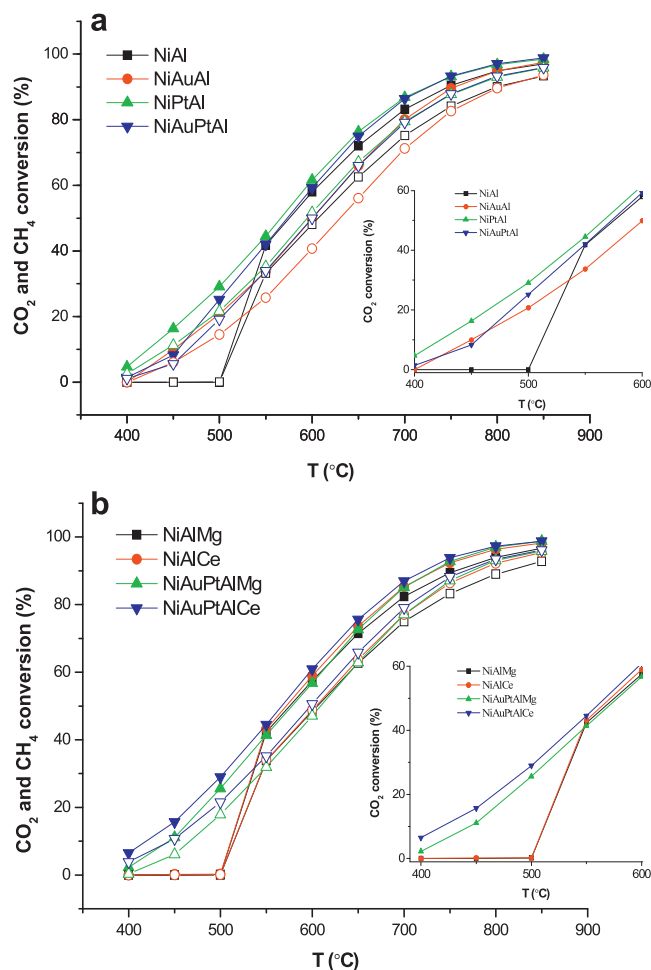


Fig. 6. CO_2 (filled symbols) and CH_4 (empty symbols) conversion percentages as function of temperature over (a) Ni-based catalysts over alumina and (b) Ni-based catalysts over doped alumina oxides. In the insets details on CO_2 conversion (%) in the range 400–600 °C are displayed. WHSV = 60,000 $\text{mL g}^{-1} \text{h}^{-1}$, feed gas composition: 15 vol% CH_4 , 15 vol% CO_2 and 70 vol% He .

Table 4

Conversions (%) of CH₄ (C_{CH₄}) and CO₂ (C_{CO₂}) and CO selectivity for the DRM over various catalysts with different temperatures: reaction conditions: CH₄/CO₂ = 1, WHSV = 60,000 mL g⁻¹ h⁻¹, 1 atm.

Catalysts	650 °C			700 °C			750 °C			800 °C		
	C _{CH₄}	C _{CO₂}	S _{CO} ^a	C _{CH₄}	C _{CO₂}	S _{CO}	C _{CH₄}	C _{CO₂}	S _{CO}	C _{CH₄}	C _{CO₂}	S _{CO}
NiAl	62.57	71.99	0.80	75.15	83.21	0.78	84.13	90.47	0.77	90.09	94.87	0.77
NiAlMg	62.68	71.45	0.80	74.95	82.38	0.79	83.26	89.43	0.78	89.04	93.97	0.77
NiAlCe	63.82	73.60	0.80	77.08	85.29	0.78	86.44	92.41	0.77	92.25	96.35	0.76
NiAuAl	56.06	65.95	0.82	71.25	80.07	0.80	82.64	89.58	0.78	89.65	94.89	0.77
NiPtAl	67.14	76.34	0.80	79.48	86.81	0.78	87.71	93.14	0.77	93.01	96.82	0.76
NiAuPtAl	65.95	74.94	0.81	79.18	86.39	0.79	87.85	93.26	0.78	93.27	97.10	0.77
NiAuPtAlMg	62.89	72.62	0.82	77.10	85.14	0.80	87.10	92.82	0.78	93.05	97.03	0.78
NiAuPtAlCe	65.84	75.57	0.80	79.06	86.94	0.78	88.24	93.84	0.77	93.41	97.26	0.77

^a CO selectivity = CO yield/(C_{CO₂} + C_{CH₄}) × 100%.

3.3. Catalytic performances

Catalytic activity of the catalysts was measured in terms of CO₂ and CH₄ conversions (%) as a function of temperature (see Fig. 6 and Table 4). In the case of bi- and tri-metallic Ni based catalysts the reaction started at around 400 °C with the conversion gradually rising with temperature. For all the monometallic Ni catalysts no activity was observed up to 500 °C followed by an abrupt increase of the conversion until ~100% at 850 °C.

For sake of simplicity only the CO₂ curves are plotted vs temperature in the insets of Fig. 6 (the trend of CH₄ curves being similar). The main effect of noble metals (Au, Pt or both) addition to Ni was, therefore, the increased CO₂ and CH₄ conversions at low temperature. Moreover, bi- and tri-metallic catalysts maintained slightly higher activity than the monometallic samples in the overall range of temperature investigated. The observed improvement of activity may be ascribed to the formation of well dispersed Au-Ni (Pt-Ni, Ni-Au-Pt) bulk alloyed active phases (as suggested by XRD analysis) and/or to synergistic interaction between nanosized metals (see before paragraph 3.6.1 TEM observation).

The CH₄ and CO₂ conversion curves were quite similar for NiAuPt catalysts independently on the undoped or doped alumina (Fig. S2). It is worth noting that the CO₂ conversion values were for all the catalysts slightly higher than those of CH₄, suggesting the occurrence of side reactions, such as the reverse water-gas shift (RWGS) and/or the CO₂ dissociation.

The selectivity values to CO (S_{CO}) was calculated at selected temperatures, in the range 650–800 °C, and are listed in Table 4. A slight decrease of CO selectivity by increasing the temperature was observed likely due to parallel reactions occurring at high temperatures, such as the decomposition of methane or steam reforming of methane with water produced by RWGS [9,39].

From the experimental results displayed in Table 4 and Fig. 6 it can be observed that the values of CH₄ conversions over our mono-, bi- and tri-metallic Ni catalysts are always less than those of equilibrium conversions reported by Amin et al. who performed the thermodynamic equilibrium analysis for DRM in view of carbon formation [40]. This finding suggests that the investigated catalysts show, under the experimental conditions used, relatively high resistance to carbon deposition in the range of temperature investigated. As it concerns the CO₂ conversion, the values are higher than the equilibrium ones for all catalysts, especially for bi- and tri-metallic samples, in the entire range of temperature investigated except at 500 and 550 °C [40]. These results are in good agreement with the researches by Wisniewski et al. [41] who found no carbon deposition over Ir/Ce_{0.9}Gd_{0.1}O_{2-x} catalysts and support the hypothesis that dissociation of CO₂ to CO and chemisorbed O species able to oxidize carbon, occurs mainly for bi- and tri-metallic Ni catalysts.

Catalytic stability of the bi-/trimetallic catalysts over alumina was also investigated as shown in Fig. 7. Compared with the NiAl and

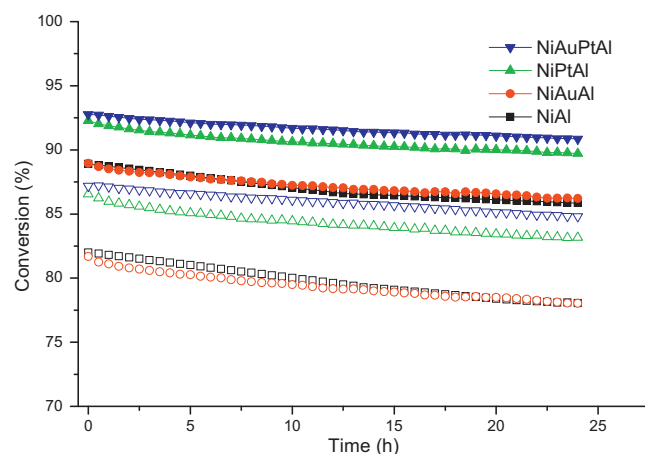


Fig. 7. Activity performance of Al supported catalysts in 24 h long-run tests at 750 °C: filled symbols CO₂ conversion, and empty symbols CH₄ conversion.

NiAuAl, NiPtAl and NiAuPtAl samples exhibit higher conversion and slightly better stability during the time-on-stream at 750 °C with a superior performance of the trimetallic systems as compared to the corresponding NiPt bimetallic catalysts. It is worth to notice that the addition of Pt to the Ni monometallic catalysts results in an enhancement of the catalytic performance, whereas addition of Au is rather neutral except for a slight improvement of the long-run stability.

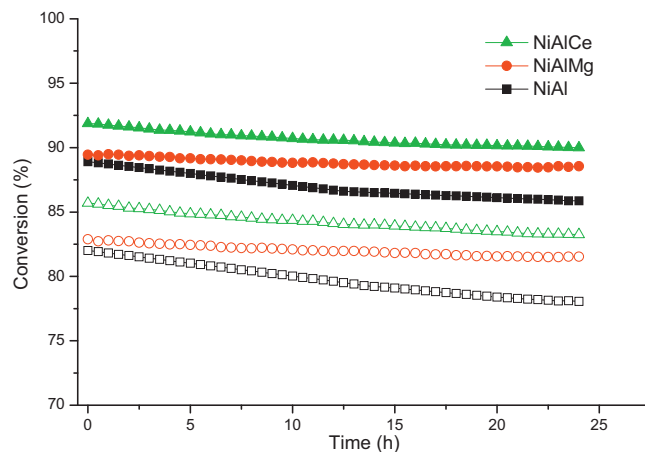


Fig. 8. Activity performance of the monometallic Ni catalysts over alumina and doped alumina, in 24 h long-run tests at 750 °C: filled symbols CO₂ conversion, and empty symbols CH₄ conversion.

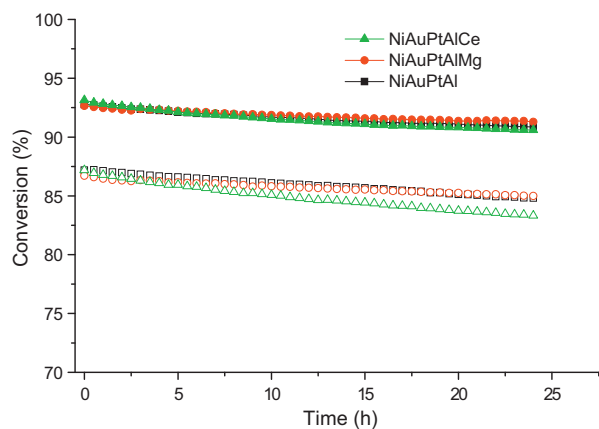


Fig. 9. Activity performance of the trimetallic catalysts over alumina and doped alumina in 24 h long-run tests at 750 °C: filled symbols CO₂ conversion, and empty symbols.

On the contrary, as observed in Fig. 8 the support composition seems to play a role on the activity of the monometallic Ni catalysts. It should be noted that whereas in the case of the NiAl the CO₂ and CH₄ conversion decrease by 3.42% and by 4.84%, respectively after 24 h, in the cases of the promoted supports the addition of Ce and to a less extent the addition of Mg improve the activity and the stability of the supported Ni catalysts over the 24 h testing period. Catalytic long-run stability tests of trimetallic catalysts doped with Mg or Ce are presented in Fig. 9. It can be clearly observed that all of the trimetallic catalysts behave similarly, regardless the support dopant, suggesting a dominant role of the metals as compared to the support.

It is well known that the addition of CeO₂ to NiAl increases the catalytic conversion, stability and coking resistance in DRM [42]. These effects are attributed to the nature of the promoter and the interaction between metal and promoter [14,15]. The CeO₂ has a redox behaviour and high mobility of lattice oxygen, which contribute to the catalytic reactivity of CeO₂ in oxidation reaction. H₂-TPR results show that the reducibility of NiAl is increased by the addition of CeO₂. From Fig. 5, the broad β reduction peak appears in NiAlCe, suggesting that the reducibility of NiAl is enhanced by the addition of Ce due to the existence of interaction between NiO and CeO₂ species. The presence of such metal-support interaction may prevent the formation of larger ensembles necessary for carbon deposition. In addition, as recently reported [43], the interaction between CeO₂ and Al₂O₃ to form CeAlO₃ phase also influences the catalytic performance of Ni supported catalysts (see later, section 3.4). Indeed, the CeAlO₃ catalyses CO₂ decomposition yielding active oxygen atoms able to oxidize carbon species arising from methane decomposition. Therefore less carbon deposition occurs over Ni/CeAlO₃ catalysts [43].

Concerning the MgO effect on the catalytic activity, it has been well documented that when all NiO particles diffuse into MgO lattice to form a NiO-MgO solid solution, the reduced catalyst would show stable and high activity in DRM [3,4,26–29]. However, our present experimental data (XRD and H₂-TPR results) could not give any evidence of the existence of the NiO-MgO solid solution in our catalysts. XRD results (see later) show that the average particle size of Ni⁰ for NiAlMg is smaller than that for NiAl after long-run test, suggesting that a relatively strong interaction between Ni⁰ and support exists in the former system. It could be inferred that such metal support interaction along with the presence of the basic MgO oxide on the surface increase the catalyst resistance towards carbon poisoning, as confirmed by low percentage of carbon (EDX/SEM).

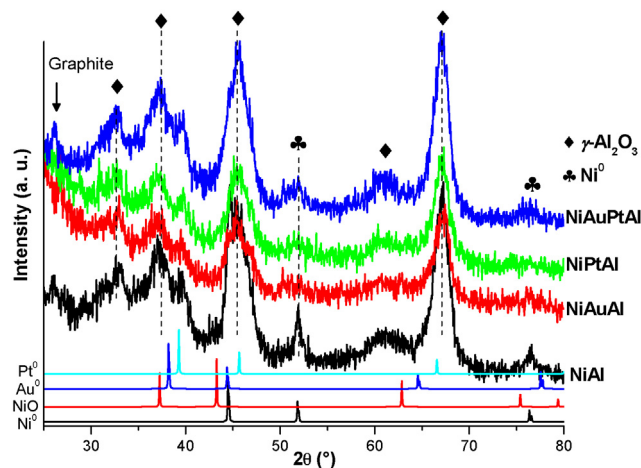


Fig. 10. XRD patterns of the alumina Ni and Ni-Au/Pt spent catalysts after long run tests.

Indeed, preferentially CO₂ chemisorption on the surface of the basic oxides should remove carbon through gasification reaction [8,39].

3.4. The XRD characterization of the catalysts after long-run tests

The XRD patterns of the bi-/trimetallic Ni-based catalysts over alumina and doped alumina were registered after long-run tests. In all cases, the XRD diffraction peaks of the metallic Ni are well evident at $\sim 44.6^\circ$ for Ni(111) and at $\sim 52^\circ$ 2θ for Ni(200) lines, respectively. According to what previously observed for reduced Ni-based catalysts (Fig. 3), the addition of Au or/and Pt or both metals leads to broadening of the Ni(200) peak along with a shift towards lower angles. No features of the Ni (111) appeared in the bi-/trimetallic catalysts, likely due to overlapping with alumina peaks. In Fig. 10 the XRD patterns of the spent Ni and Ni-Au/Pt alumina catalysts are displayed as an example, while the diffraction curves of NiAuPtAlMg and NiAuPtAlCe showing the similar broadening and shift of the Ni (200) peak are not shown for sake of brevity. These findings suggest that the addition of Au or/and Pt prevents the sintering of metallic Ni during long-run tests performed at high temperature for 24 h. It can be speculated that in the bi- and tri-metallic catalysts some bulk alloy formation may occur as well as synergistic interactions between close metallic nanoparticles cannot be excluded. On the contrary, the particle size of the Ni⁰ of the monometallic catalysts suffers slight increase. The average particle size calculated by the Scherrer equation, and Ni⁰ dispersion assuming spherical and uniform particles for the spent catalysts, are shown in Table S3. In addition, graphite carbon (JCPDS 89-8491) diffraction peaks are also observed in the patterns of the spent catalysts.

The XRD patterns of monometallic catalysts doped with Mg or Ce after long-run test are presented in Fig. 11. In this series of the spent catalysts, the average particle size of Ni⁰ follows the order of NiAl (12.9 nm) > NiAlCe (12.3 nm) > NiAlMg (10.8 nm). The XRD pattern of the spent NiAlMg does not present any new Al₂O₃-MgO phase with respect to that of the calcined NiAlMg. While, the spent NiAlCe contains a new phase CeAlO₃ formed under reduction atmosphere, not observed in the calcined NiAlCe [43,44]. The above results suggest that the catalytic stability is likely related to the support effect and does not depend on the Ni particle size.

3.5. XPS analysis

XPS technique was used to study the surface chemical composition of the catalysts. Because of the impossibility to reduce “in

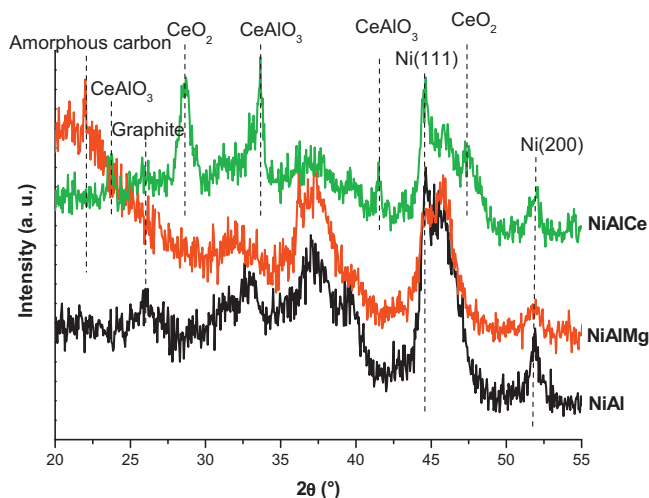


Fig. 11. XRD patterns of the Ni catalysts over alumina and alumina doped with Mg or Ce after long-run test.

situ” the catalysts before analysis, the measurements were carried out over selected catalysts after calcinations, while no measurements over reduced samples are hereinafter reported. The attempt to record a XPS spectrum of the catalyst NiAuPtAl immediately after reduction at 750 °C and storage under He has highlighted an immediate re-oxidation of some metallic Ni. In order to get insight into the surface composition, sintering and or poisoning of active species after catalytic tests, analyses of spent catalysts were also performed.

The binding energy values and the XPS derived atomic ratios are summarized in Table 5 for Ni 2p_{3/2}. Unfortunately the Au and Pt main peaks overlap with the Al 2p photoelectron peak and, due to their low concentration, they are not visible. Fig. 12 shows the Ni 2p photoelectron spectra of the calcined and after long-run NiAuPtAl sample, as example. In the figure the experimental and the curve fitted spectra are shown. The spectrum of the calcined sample is typical of Ni²⁺ state with the characteristic two spin orbit components Ni 2p_{3/2} and Ni 2p_{1/2} separated by ~17–18 eV and the two shake up satellite peaks located at about 6 eV higher energy with respect to the main photoelectron peaks. For all calcined samples the Ni 2p_{3/2} binding energy ranges at 855.3 ± 0.2 typical of oxidized nickel. The pure NiO is generally characterized by a binding energy of 854.5 eV. The value obtained in the present samples was intermediate between the bulk NiO and the spinel NiAl₂O₄ characterized by a Ni 2p_{3/2} binding energies of 856 eV [45], indicating a high interaction with the support, consistent with the results of H₂-TPR (Fig. 4). For all calcined Ni-based catalysts, the Ni/Al atomic ratio was close to the nominal one, suggesting a relatively high dispersion of the

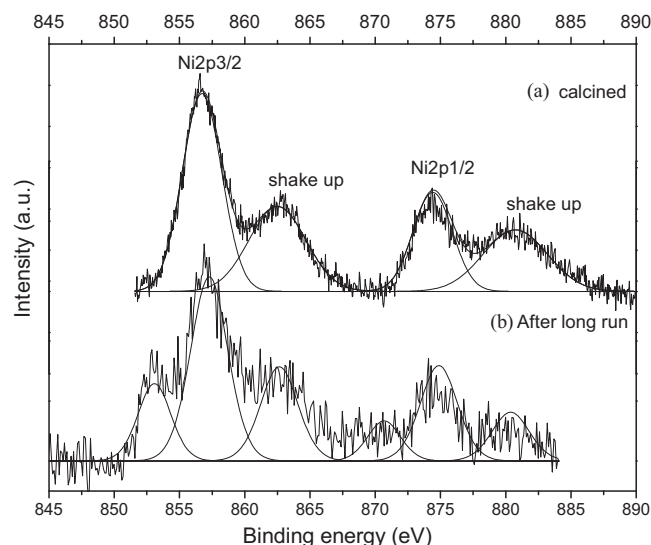


Fig. 12. Ni 2p high resolution XPS region for the NiAuPtAl catalyst after different treatments: (a) calcination and (b) after long run.

Ni particles over the alumina support, even after Au/Pt deposition and further calcination. An exceptionally high amount of Ni was detected on NiAlMg, suggesting a very good dispersion of Ni active species over the support surface. This finding is in agreement with the highest surface area measured for AlMgO oxide that did not suffer any shrinkage after Ni deposition (see Table S1).

After long-run test, along with the oxidized components appears a new doublet whose position range between 851.5 and 853.2 eV. The large range of this position is due to the low intensity of the Ni 2p_{3/2} peaks and the consequent low quality of the fitting, nevertheless we attributed these new peaks to metallic nickel [46].

According to the XPS analyses of the samples after long-run test a significant reduction of the Ni/Al atomic ratio was observed. Such change may reflect either a decrease of the surface nickel content due to an increase of the nickel particle size, either an inward diffusion of nickel, or coverage of the nickel particle by another chemical species, such as carbon. The highest Ni/Al atomic ratio was observed again for NiAlMg after long-run, confirming the highest dispersion of Ni particles in such catalyst likely due to strong metal-support interaction. Moreover, in the case of Ce doped catalysts an increase of Ce³⁺/Ce⁴⁺ ratio was observed after long run consistent with the formation of CeAlO₃ observed by XRD.

In order to clarify if Ni sintering and/or coverage of Ni particles occurred upon long-run tests, the XPS analysis of the NiAl sample after long-run followed by TPO to 1000 °C was performed. As shown in Table 5 after long-run Ni peak was so low that was not possible

Table 5
Binding energies (eV) and surface atomic ratios of selected catalysts after calcination and long-run test.

Catalysts	Calcined at 550 °C			After long-run test		
	Ni 2p _{3/2}	Ni/Al (theoretical 0.036) M = (Mg/Ce)	M/Al ^a	Ni 2p _{3/2}	Ni/Al	M/Al (M = Mg/Ce)
NiAl	855.2	0.035		n.d.	n.d.	
NiAuAl	855.5	0.029		853.2 (35%)855.9 (65%)	0.018	
NiPtAl	855.4	0.029		852.6 (50%)856.5 (50%)	0.017	
NiAuPtAl	855.3	0.031		851.5 (20%)855.0 (80%)	0.026	
NiAlMg	855.3	0.049	0.05 (0.15)	853.3 (24%) 855.6 (74%)	0.032	0.03 (0.15)
NiAlCe	855.5	0.025	0.02 ^b (0.04)	853.3 (29%) 855.6 (71%)	0.014	0.03 ^c (0.04)

^a In parenthesis theoretical value.

^b Ce³⁺ (%) = 7%.

^c Ce³⁺ (%) = 16%.

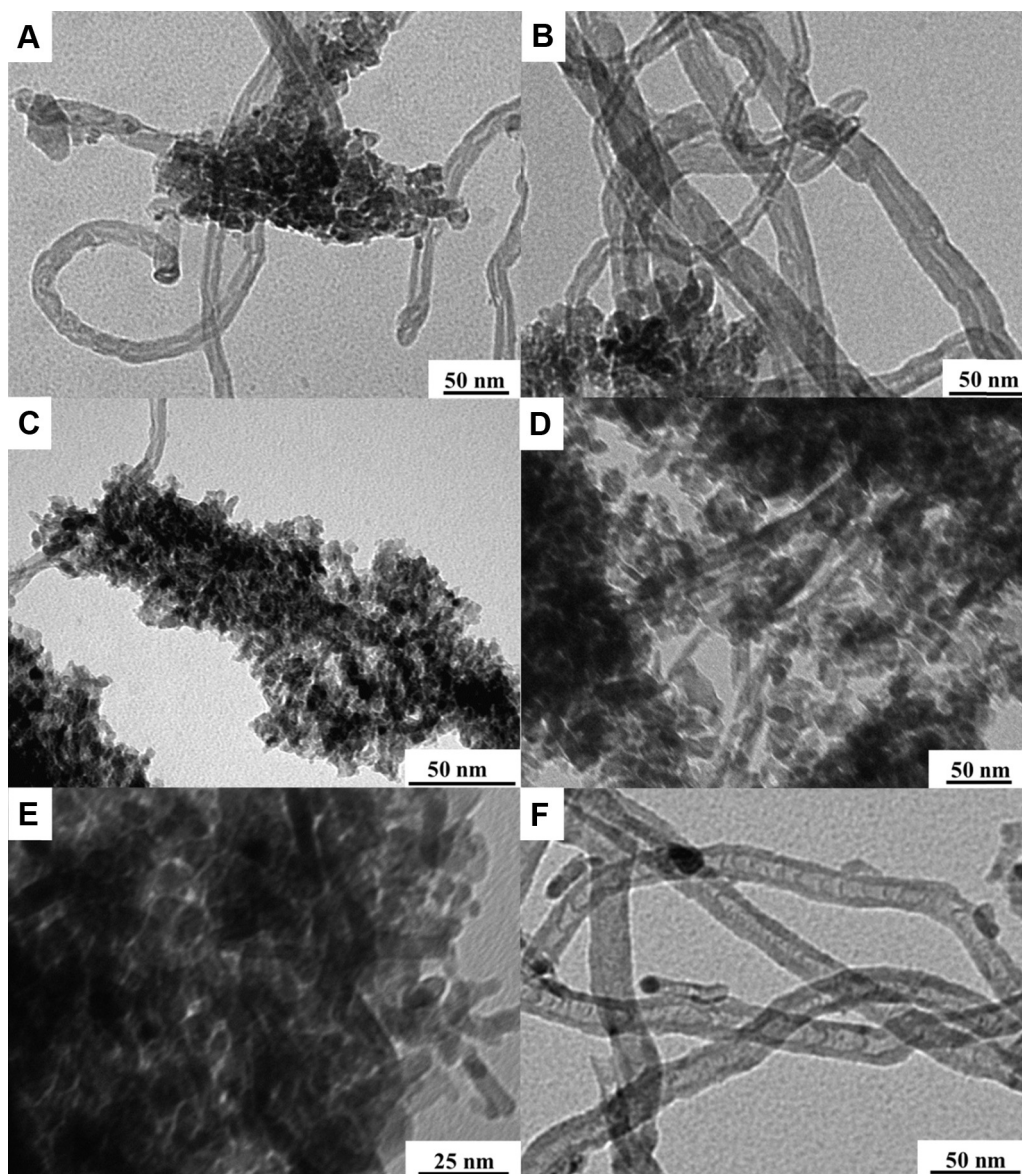


Fig. 13. TEM images (with high magnification) of selected catalysts after long run: NiAl (A); NiAlCe (B), NiAlMg (C), NiAuAl (D), NiPtAl (E), NiAuPtAl (F).

to quantify. After the TPO treatments the Ni/Al values increased to 0.026, indicating that the removed carbon was deposited on nickel sites. By comparing this result with the other characterization on the spent samples we can attribute the decrease of the Ni/Al ratio in the spent samples mainly to carbon deposition.

Although, as stated before, the Pt 4f peak overlap with the Al 2p, we observed a not-quantifiable surface segregation of Pt after long-run treatment, as shown in Fig. S3. The Pt 4f_{7/2} binding energy (72.7 eV) was attributable to Pt²⁺ [47,48]. The result suggests the presence of metal-support interaction, i.e., the electron transfer between the Pt and the support or nickel can be involved in trimetallic catalysts.

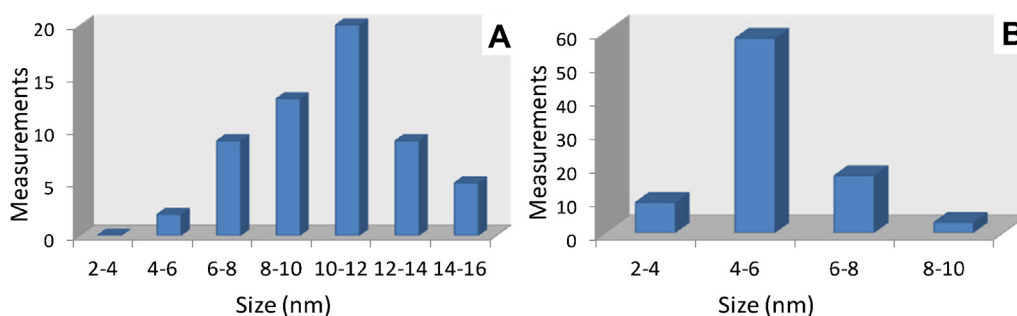
On the basis of structural and surface characterization data so far discussed, the catalytic behaviour of the catalysts would be related to bulk alloy formation (as supposed by XRD), small particle size of active sites, and synergistic interaction between distinct Ni and Au/Pt metals. XRD results suggest that the formation of the Au-Ni, Pt-Ni, and Ni-Au-Pt alloys takes place after H₂ reduction. Simultaneously, the particle size of such alloyed and synergistically interacting Ni-based active sites decreases as confirmed by XRD and TEM analyses (see above). TPR results show that in all

trimetallic catalysts (calcined ones) the existence of the β peaks could be due to both an interaction among Au, Pt and Ni species, which could increase the reducibility of NiO. In agreement with the mentioned interaction between noble metals and Ni species, XPS results show that in the bi-/trimetallic catalysts the proportion of Ni⁰ (>20%, spent ones) is higher than that in the 5 wt%Ni monometallic catalyst (14%, reduced one) reported in literature [49]. Moreover, the surface Ni/Al ratio for the trimetallic catalysts is higher than those for the mono-/bimetallic catalysts after long-run tests. This phenomenon could be explained by the fact that Au-Pt addition promoted higher dispersion of Ni over alumina.

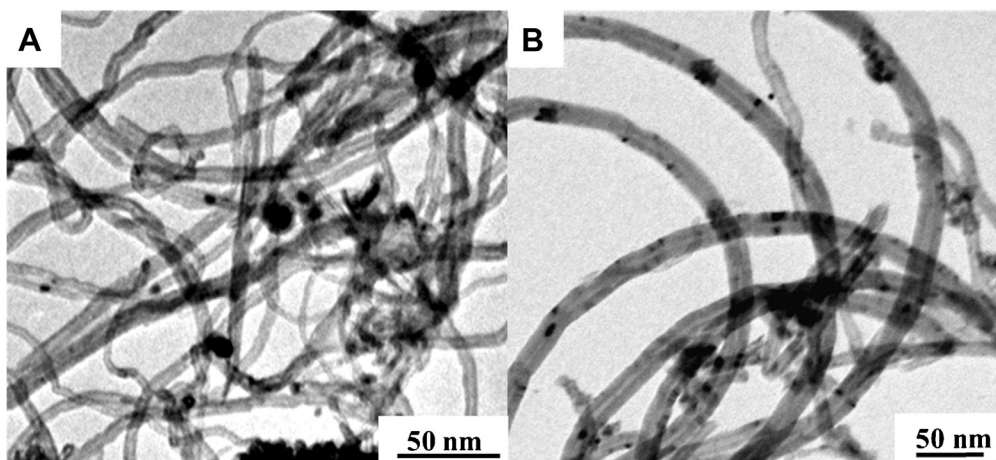
3.6. Structure of carbon deposits and carbon amount

3.6.1. TEM observation

In order to have a better understanding of the catalytic differences between the various catalysts, a careful microscopic investigation was performed on all the samples after long-run tests at 750 °C. A first screening performed by means of transmission electron microscopy revealed a clear difference in terms of carbonaceous species present on the surface of the catalysts after long-run



a. Particle size distributions for the NiAl (A) and NiAuPtAl (B) catalysts after long run.



b: TEM images of NiAl (A) and NiAuPtAl (B) evidencing the catalysts particles size.

Fig. 14. (a) Particle size distributions for the NiAl (A) and NiAuPtAl (B) catalysts after long run. (b) TEM images of NiAl (A) and NiAuPtAl (B) evidencing the catalysts particles size.

experiments. It is known that the presence of coke has a detrimental influence on the catalytic performances. Among the other possible carbon species (amorphous carbon, crystalline graphite and filaments) the ones that are better tolerated and did not causes major deactivation are the filamentous carbon residues. TEM measurements revealed, as expected, that the most active catalysts are the ones presenting the carbonaceous species in the form of nanotubes on the surface (NiAuPtAl and NiAlCe). Generally, we have observed that nature of carbon deposits and their relative amount depend on the type of catalyst (active metals and/or support type). In details, for the monometallic NiAl catalyst (Fig. 13, image A), there are at least two types of carbon, *i.e.*, amorphous carbon and carbon nanotubes. The NiAlMg as well as the bimetallic (Ni-Au/Pt) catalysts present, after long-run tests, a high amount of amorphous carbon (Fig. 13, images C, D and E). In the case of NiAlCe carbonaceous species in the form of nanotubes were also observed (Fig. 13, image B), while a nice bamboo-like structure was detected for Ni-Au-Pt trimetallic catalyst (Fig. 13, image F).

This interesting structural difference concerning the carbon filament could suggest the formation of nickel alloys with gold and platinum rather than separate metal nanoparticles in the NiAuPtAl sample. The formation of alloys could preferentially generate the bamboo-like carbon structures and catalyze carbon gasification. In order to prove this hypothesis the particles size distribution of the NiAuPtAl sample was estimated and compared with the analogous catalyst bearing Ni nanoparticles without gold and platinum (NiAl). The formation of alloys should lead to smaller metallic aggregates.

In Fig. 14a the particle size distributions for NiAl and NiAuPtAl after long run are displayed. In Fig. 14b two representative TEM images with high magnification are shown. It is clear that the

trimetallic NiAuPtAl is characterized by a narrower particle size distribution and by the presence of smaller metallic nanoparticles. The average values for the samples NiAuPtAl and NiAl calculated by electron microscopy (corresponding to 5.3 and 10.5 nm, respectively) is in good accordance with the particle size calculated by using the Scherrer equation (Table 2). The catalytic difference between the two samples NiAl (the less active) and the NiAuPtAl (the most active) could be ascribed to the formation of alloyed and/or synergically interacting nanoparticles that beside the increased activity in methane reforming presents the additional advantage of produce less amount of total carbonaceous residues. Quantification of the total carbon performed by means of X-ray microanalysis realized with the scanning electron microscope confirm that NiAl presents a higher amount of carbon (19 mass% for the NiAl sample compared 9 mass% for NiAuPtAl sample) compared with the analogous NiAuPtAl. A lower carbon amount with respect to NiAl was also observed on the spent monometallic NiAlMg and NiAlCe catalysts (10 and 12 mass%, respectively). The carbon content for the monometallic and trimetallic catalysts determined by EDX microanalysis is reported in Table 6.

Table 6

Carbon content for the monometallic and trimetallic catalysts determined by EDX microanalysis.

Samples	%C
NiAl	18.96
NiAlMg	9.05
NiAlCe	12.05
NiAuPtAl	9.48

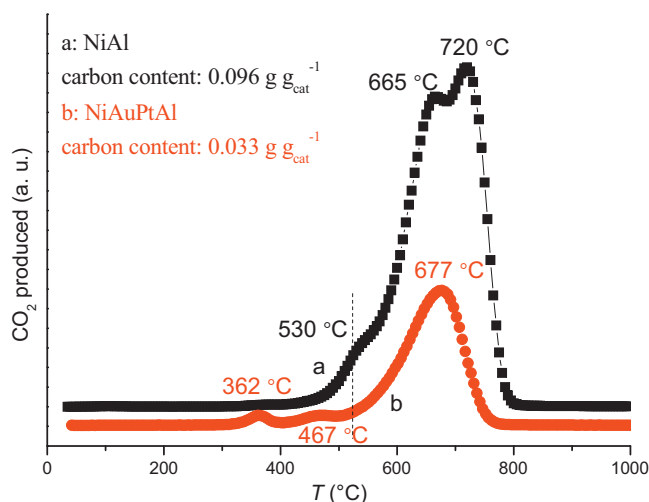


Fig. 15. TPO profiles of the NiAl and NiAuPtAl catalysts after long-run tests.

From what observed by microscopic characterization it appears clear that there is a strong correlation between catalytic activity and typology/amount of carbonaceous species. The best catalysts (NiAuPtAl and NiAlCe) are the ones with the better combination of these two parameters (high amount of carbon nanotubes together with low quantity of total carbon).

3.6.2. O₂-TPO analysis

Typical O₂-TPO profiles were performed to study the reactivity of the carbon deposits formed on the two selected spent catalysts (see Fig. 15). For the spent NiAl, there are two main peaks located at 720, 665°C and one shoulder appears at 530°C. While for the spent NiAuPtAl one main peak appears at 677°C and two low-intensity peaks are found at 467 and 362°C, respectively. It has been suggested that Ni-based catalysts are active for the oxidation of carbon species, and the oxidation temperature of the carbon species can be affected by the nature of carbon and catalysts, and interaction between the carbon and the Ni particles [50]. In other words, the oxidation temperature of the carbon encapsulated Ni particles would be quite high because the oxygen molecules or atoms cannot attach to and activated by the Ni particles. For example, the temperature of oxidation of graphitic carbon is about 725°C without a Ni catalyst [50]. For the spent NiAl, the peak at 720°C may be caused by the oxidation of the graphitic carbon covering or encapsulating the Ni nanoparticles. The peak at 665°C is probably originated from the oxidation of the filamentous carbon. Finally, the peak at 530°C is attributed to amorphous carbon due to its relatively low oxidation temperature compared with the graphitic one.

For the spent NiAuPtAl the main peak centred at 677°C is assigned to the oxidation of bamboo-like carbon nanotubes. The peaks at 362 and 467°C may represent the oxidation of the amorphous carbon covering Ni particles. The TPO profiles show that the amount of carbon deposited in the spent NiAuPtAl is much less than that in the spent NiAl, indicating an enhanced resistance of the NiAuPtAl to coking, consistent with the results of X-ray microanalysis. It is also clear from Fig. 15 that the maximum O₂-TPO peak temperature of the carbon deposited on the NiAuPtAl shows a considerable reduction as compared with that for NiAl. It can be rationally inferred that the presence of Ni-Au-Pt alloy is able to activate the O₂ thereby promoting the low-temperature oxidation of the carbon deposits.

3.7. Relationship between catalyst composition and carbon deposits

XRD results suggest formation of Au-Ni, Pt-Ni, and Ni-Au-Pt bulk alloys after H₂ reduction. Simultaneously, the particle sizes of the Ni bi-trimetallic catalysts are smaller in comparison with the monometallic samples, as confirmed by XRD and TEM. The TPR patterns of the calcined samples show the presence of a strong β peak in the trimetallic catalysts, except the one on Mg doped alumina. Such peak indicates an easier reducibility of the nickel oxide likely due to some synergistic interaction between NiO and the Au/Pt dopants.

The TEM and TPO results of our spent catalysts provide clear evidence of carbon deposits during the reforming reaction. It should be noted that the morphology and amount of the carbon is essentially affected by the composition of the catalysts. Two types of carbon, i.e., the amorphous carbon and the nanotubes, are observed by TEM on the surface of the Ni catalysts supported over alumina. However, the surface carbon on spent NiAuAl and NiPtAl is dominated by amorphous carbon, while the NiAuPtAl catalyst evidences mostly the bamboo-like nanotubes. Pawelec et al. postulated that size of Ni particles could influence the morphology of the carbon [49]. They found that graphite-like carbon and a very small amount of filamentous carbon were detected on the surface of the bimetallic Pt-Ni catalyst. Moreover, filamentous carbon increased after increasing the Ni content, i.e., increasing the particle size of Ni. Similar results have been reported by other authors [51].

On the basis of our experimental data and of the models suggested in the literature [52], the following model may be used to explain the growth of the carbon on the surface of our selected catalysts. It is generally accepted that the CH₄ molecules are decomposed on nickel surface to reactive species CH_x (x=0–3), while the CO₂ molecules are chemisorbed and dissociated on metal surface, or form carbonate-like species on support surface [43]. The gasification of adsorbed carbon from CH₄ fragments is thought to proceed on nickel surface as well as at the boundary of nickel-support. Isolated carbon atoms, which are not gasified immediately, will diffuse through the nickel surface to reach the nickel-support interface. Depending on the active sites, the carbon atoms generated on the catalyst surface have different mobility and assemble into hexagonal and pentagonal rings [53]. A graphite layer is composed of the hexagonal carbon rings. The pentagonal carbon rings introduce changes in the curvature of graphitic flake to accommodate the geometry of the interior layers [53]. One can make structural models of nanotubes and bamboo-like nanotubes based on geometrical combinations of these carbon rings. Therefore, one can assume that over the NiAl, characterized by larger metal particles, the mobility of surface carbon is relatively low, and a geometrical combination of hexagonal rings results in the formation of nanotubes. On the surface of the bimetallic catalysts, the reactivity on metal-support boundary may be higher than that for the monometallic catalyst. The isolated carbon atoms will be gasified immediately and the nucleation and growth of nanotubes will be hampered. Thus, only a very low amount of nanotubes can be observed by TEM. When the trimetallic catalyst is used, it can be speculated that there is an enhanced mobility of surface carbon atoms, probably due to the smaller particle sizes and the increased grain boundaries, and the formation of pentagonal rings becomes favourable. The introduction of pentagonal rings into the clusters of carbon should change the curvature of graphitic flake, thus facilitating the formation of bamboo-like nanotubes.

Because of the complexity of the growth processes, further research is needed to better understand the relationship between the nature of NiAuPt active sites and the morphology of carbon.

4. Conclusions

On the basis of the characterization and catalytic performance data the following conclusions can be drawn: (i) the presence of a small amount of Au or/and Pt (0.2 wt%) in bi-/trimetallic catalysts affects the structural and reduction property. In details, addition of Au and Pt leads to formation of nanosized Ni particles synergistically interacting with Au/Pt. Alloyed NiAuPt phases are also postulated on the basis of XRD characterization. This kind of interaction leads to both effects, enhanced reduction of NiO species and improved catalytic performance of the bi-/trimetallic catalysts. The carbon formation on the surface of the catalysts depends on the composition of the active sites (NiAu, NiPt, NiAuPt). Moreover, a direct relation between catalytic activity and typology/amount of carbonaceous species was found. The best catalysts (NiAuPtAl and NiAlCe) are the ones with the better combination of these two parameters (high amount of carbon nanotubes together with low quantity of total carbon).

Alumina modification with the basic MgO or CeO₂ significantly improves the catalytic performance of the monometallic Ni catalyst but does not influence the performance of the trimetallic catalysts.

Acknowledgements

The authors acknowledge the financial support provided by Italy, EFOR-CNR Project (Energies by Renewable sources) and by European Community, COST Action CM 1104. Dr. Francesco Giordano from ISMN-CNR is gratefully acknowledged for XRD measurements.

The China Scholarship Council is sincerely acknowledged for supporting Wu's scholarship. H.J. Wu thanks the Excellent Doctorate Foundation, Doctorate Foundation of Northwestern Polytechnical University and the Scholarship Award for Excellent Doctoral Student granted by Ministry of Education, P.R. China.

Appendix A. Supplementary data

Supplementary data associated with this article can be found, in the online version, at <http://dx.doi.org/10.1016/j.apcatb.2014.03.018>.

References

- [1] N. Wagstaff, R. Prins, *J. Catal.* 59 (1979) 434–445.
- [2] C. Raab, J.A. Lercher, J.G. Goodwin, J.Z. Shyu, *J. Catal.* 122 (1990) 406–414.
- [3] Y.G. Chen, O. Yamazaki, K. Tomishige, K. Fujimoto, *Catal. Lett.* 39 (1996) 91–95.
- [4] Y.G. Chen, K. Tomishige, K. Yokoyama, K. Fujimoto, *Appl. Catal. A* 165 (1997) 335–347.
- [5] Ş. Özkara-Aydinoğlu, A.E. Aksoylu, *Int. J. Hydrogen Energy* 36 (2011) 2950–2959.
- [6] M. García-Diéguez, I.S. Pieta, M.C. Herrera, M.Á. Larrubia, L.J. Alemany, *J. Catal.* 270 (2010) 136–145.
- [7] M. García-Diéguez, E. Finocchio, M.Á. Larrubia, L.J. Alemany, G. Busca, *J. Catal.* 274 (2010) 11–20.
- [8] L. Gucci, G. Stefler, O. Geszti, I. Sajó, Z. Pászti, A. Tompos, Z. Schay, *Appl. Catal. A* 375 (2010) 236–246.
- [9] A. Horváth, L. Cuczi, A. Kocsonya, G. Sáfrán, V. La Parola, L.F. Liotta, G. Pantaleo, A.M. Venezia, *Appl. Catal. A* 468 (2013) 250–259.
- [10] K. Nagaoka, K. Seshan, K. Aika, J.A. Lercher, *J. Catal.* 197 (2001) 34–42.
- [11] K. Nagaoka, M. Okamura, K. Aika, *Catal. Commun.* 2 (2001) 255–260.
- [12] H.Y. Wang, E. Ruckenstein, *Appl. Catal. A* 204 (2000) 143–152.
- [13] N. Al-Yassir, R. Le Van Mao, *Appl. Catal. A* 317 (2007) 275–283.
- [14] A. Caballero, J.P. Holgado, V.M. Gonzalez-delacruz, S.E. Habas, T. Herranz, M. Salmeron, *Chem. Commun.* 46 (2010) 1097–1099.
- [15] V.M. Gonzalez-Delacruz, F. Terner, R. Pereñíguez, A. Caballero, J.P. Holgado, *Appl. Catal. A* 384 (2010) 1–9.
- [16] A.M. Efstathiou, A. Kladi, V.A. Tsipourari, X.E. Verykios, *J. Catal.* 158 (1996) 64–75.
- [17] P. Ferreira-Aparicio, I. Rodriguez-Ramos, J.A. Anderson, A. Guerrero-Ruiz, *Appl. Catal. A* 202 (2002) 183–196.
- [18] A. Slagtern, J. Schuurman, C. Leclercq, X. Verykios, C. Mirodatos, *J. Catal.* 172 (1997) 118–126.
- [19] Z. Zhang, X.E. Verykios, S.M. Macdonald, S. Affrossman, *J. Phys. Chem.* 100 (1996) 744–754.
- [20] K. Tomishige, Y. Chen, K. Fujimoto, *J. Catal.* 181 (1999) 91–103.
- [21] S.B. Tang, F.L. Qiu, S.J. Lu, *Catal. Today* 24 (1995) 253–255.
- [22] T. Horiuchi, K. Sakuma, T. Fukui, Y. Kubo, T. Osaki, T. Mori, *Appl. Catal. A* 144 (1996) 111–120.
- [23] S. Wang, G.Q. Lu, *J. Chem. Technol. Biotechnol.* 75 (2000) 589–595.
- [24] S.H. Seok, S.H. Choi, E.D. Park, S.H. Han, J.S. Lee, *J. Catal.* 209 (2002) 6–15.
- [25] J.H. Bitter, K. Seshan, J.A. Lercher, *J. Catal.* 183 (1999) 336–343.
- [26] Y.H. Wang, H.M. Liu, B.Q. Xu, *J. Mol. Catal. A* 299 (2009) 44–52.
- [27] E. Ruckenstein, Y.H. Hu, *Appl. Catal. A* 133 (1995) 149–161.
- [28] Y.H. Hu, E. Ruckenstein, *Catal. Lett.* 43 (1997) 71–77.
- [29] Y.H. Hu, E. Ruckenstein, *Catal. Lett.* 36 (1996) 145–149.
- [30] F. Gökaliler, B.A. Göçmen, A.E. Aksoylu, *Int. J. Hydrogen Energy* 33 (2008) 4358–4366.
- [31] JCPDS Powder Diffraction File, International Centre for Diffraction Data, Swarthmore, PA, USA, 1989.
- [32] H.P. Klug, L.E. Alexander, *X-ray Diffraction Procedures for Polycrystalline and Amorphous Materials*, Wiley, New York, 1954.
- [33] S.J. Gregg, K.S. Sing, *Adsorption, Surface Area and Porosity*, 2nd ed., Academic Press, San Diego, 1982.
- [34] L.F. Liotta, G. Pantaleo, G. Di Carlo, G. Marci, G. Deganello, *Appl. Catal. B* 52 (2004) 1–10.
- [35] D.A. Shirley, *Phys. Rev. B* 5 (1972) 4709–4714.
- [36] P.M.A. Sherwood, in: D. Briggs, M.P. Seah (Eds.), *Practical Surface Analysis*, Wiley, New York, 1990, p. 181.
- [37] H.P. Klug, L.E. Alexander, *X-ray Diffraction Procedures for Polycrystalline and Amorphous Materials*, Wiley, New York, 1954.
- [38] C. Li, Y.W. Chen, *Thermochim. Acta* 256 (1995) 457–465.
- [39] M.C.J. Bradford, M.A. Vannice, *Catal. Rev.: Sci. Eng.* 41 (1999) 1–42.
- [40] M.K. Nikoo, N.A.S. Amin, *Fuel Proc. Technol.* 92 (2011) 678–691.
- [41] M. Wisniewski, A. Boreave, P. Gelin, *Catal. Commun.* 6 (2005) 596–600.
- [42] S.B. Wang, G.Q. Lu, *Appl. Catal. B* 19 (1998) 267–277.
- [43] W. Chen, G.F. Zhao, Q.S. Xue, L. Chen, Y. Lu, *Appl. Catal. B* 136–137 (2013) 260–268.
- [44] T.Y. Kim, S.M. Kim, W.S. Lee, S.I. Woo, *Int. J. Hydrogen Energy* 38 (2013) 6027–6032.
- [45] B.W. Hoffer, A.D. van Langeveld, J.P. Janssens, R.L.C. Bonnè, C.M. Lok, J.A. Moulijn, *J. Catal.* 192 (2000) 432–440.
- [46] H.W. Nesbitt, D. Legrand, G.M. Bancroft, *Phys. Chem. Minerals* 27 (2000) 357–366.
- [47] S.S. Kim, H.H. Lee, S.C. Hong, *Appl. Catal. A* 423–424 (2012) 100–107.
- [48] L. Olsson, E. Fridell, *J. Catal.* 210 (2002) 340–353.
- [49] B. Pawelec, S. Damyanova, K. Arishtirova, J.L.G. Fierro, L. Petrov, *Appl. Catal. A* 323 (2007) 188–201.
- [50] P. Wang, E. Tanabe, K. Ito, J. Jia, H. Morioka, T. Shishido, K. Takehira, *Appl. Catal. A* 231 (2002) 35–44.
- [51] S.R. de Miguel, I.M.J. Vilella, S.P. Maina, D. San José-Alonso, M.C. Román-Martínez, M.J. Illán-Gómez, *Appl. Catal. A* 435–436 (2012) 10–18.
- [52] X.S. Qi, Y. Deng, W. Zhong, Y. Yang, C. Qin, C.T. Au, Y.W. Du, *J. Phys. Chem. C* 114 (2010) 808–814.
- [53] Z.C. Kang, Z.L. Wang, *J. Phys. Chem.* 100 (1996) 5163–5165.